Opto-Electronic Advances

CN 51-1781/TN ISSN (Print) 2096-4579 ISSN (Online) 2097-3993

Millisecond-level electrically switchable metalens for adaptive rotational depth mapping and diffraction-limited imaging

Yeseul Kim, Jihae Lee, Won-Sik Kim, Hyeonsu Heo, Dongmin Jeon, Beomha Yang, Xiaotong Li, Harit Keawmuang, Shiqi Hu, Young-Ki Kim, Trevon Badloe* and Junsuk Rho*

Citation: Kim Y, Lee J, Kim WS, Heo H, Jeon D, Yang B, Li XT, Keawmuang H, Hu SQ, Kim YK, Badloe T, Rho J. Millisecond-level electrically switchable metalens for adaptive rotational depth mapping and diffraction-limited imaging. *Opto-Electron Adv* **9**, 250216(2026).

https://doi.org/10.29026/oea.2026.250216

Received: 20 August 2025; Accepted: 2 December 2025; Published online: 9 February 2026

OEA | Opto-Electronic Advances

Article

February 2026, Vol. 9, No. 2

Open Access

Millisecond-level electrically switchable metalens for adaptive rotational depth mapping and diffraction-limited imaging

Yeseul Kim[1†], Jihae Lee[2†], Won-Sik Kim[2], Hyeonsu Heo[1], Dongmin Jeon[1], Beomha Yang[3], Xiaotong Li[1], Harit Keawmuang[1], Shiqi Hu[1,9], Young-Ki Kim[2], Trevon Badloe[4,5]* and Junsuk Rho[1,2,6,7,8]*

Abstract: We demonstrate an electrically tunable dual-mode metalens capable of polarization-sensitive focal control, combining high-resolution imaging and depth-sensing functionalities into a single compact device. By integrating hydrogenated amorphous silicon (*a*-Si:H) meta-atoms with a liquid crystal (LC) modulator, the proposed metasurface independently manipulates left- and right-circularly polarized (LCP/RCP) incident light, generating a rotating double-helix focal distribution for LCP and an extended depth-of-focus (DOF) for RCP illumination. The meta-atoms were rigorously optimized using propagation and geometric phases, enabling precise phase control and high transmittance at a wavelength of 635 nm. Experimental characterization confirmed near-diffraction-limited lateral and axial resolutions, closely aligning with theoretical predictions. The integrated LC cell facilitates milliseconds polarization-switching between depth-sensitive double-helix and high-resolution DOF imaging modes. We further verified depth-extraction capabilities by analyzing rotation angles from dual-image focal spots under mixed-polarization illumination. Depth-resolved imaging of a rubber-tree leaf, a skeletal-muscle cross-section, and a live planarian retrieved color-coded depths, demonstrating the effectiveness on complex biological tissues. This polarization-driven, electrically tunable metalens thus provides a versatile and effective optical platform suitable for advanced applications in biomedical imaging, three-dimensional sensing, adaptive optics, and compact imaging systems.

Keywords: chiral-dependent 3D imaging retrieval; chiral-dependent 3D imaging; spin dependent; electrically tunable; metasurface

DOI: 10.29026/oea.2026.250216 | CSTR: 32247.14.oea.2026.250216

Citation: Kim Y, Lee J, Kim WS et al. Millisecond-level electrically switchable metalens for adaptive rotational depth mapping and diffraction-limited imaging. *Opto-Electron Adv* **9**, 250216 (2026).

Introduction

Metasurfaces, composed of planar arrays of subwavelength structures known as meta-atoms, have emerged as powerful optical elements capable of precisely manipulating the amplitude, phase, and polarization of incident light[1–4]. By engineering the geometry and arrangement of individual meta-atoms, metasurfaces can achieve complex wavefront transformations with ultra-thin profiles, presenting a compact and efficient alternative to conventional bulky optical components[5–9]. In particular, metalenses, which are metasurface-based lenses, have garnered considerable attention due to their ability to focus or image light with near diffraction-limited performance while significantly reducing device volume and weight compared to traditional refractive optics[10–15].

Received: 20 August 2025

Accepted: 2 December 2025

Published online: 9 February 2026

[1]Department of Mechanical Engineering, Pohang University of Science and Technology (POSTECH), Pohang 37673, Republic of Korea; [2]Department of Chemical Engineering, Pohang University of Science and Technology (POSTECH), Pohang 37673, Republic of Korea; [3]Department of Quantum Information Science, Pohang University of Science and Technology (POSTECH), Pohang 37673, Republic of Korea; [4]Department of Electronics and Information Engineering, Korea University, Sejong 30019, Republic of Korea; [5]Division of Smart Energy Convergence Engineering, Korea University, Sejong 30019, Republic of Korea; [6]Department of Electrical Engineering, Pohang University of Science and Technology (POSTECH), Pohang 37673, Republic of Korea; [7]POSCO-POSTECH-RIST Convergence Research Center for Flat Optics and Metaphotonics, Pohang 37673, Republic of Korea; [8]National Institute of Nanomaterials Technology (NINT), Pohang 37673 Republic of Korea; [9]Platform for Real-world Innovation in Smart Manufacturing and AI, Korea Advanced Institute of Science and Technology (KAIST), Daejeon, 34141, Republic of Korea.

†These authors contributed equally to this work.

*Correspondence: T Badloe, E-mail: trevon@korea.ac.kr; J Rho, E-mail: jsrho@postech.ac.kr

Despite these advantages, conventional metasurfaces typically operate under fixed optical conditions, such as a predefined wavelength, polarization, or incidence angle. To address this limitation, significant efforts have been made to realize dynamically tunable metasurfaces[16–20]. Various modulation strategies have been investigated, including mechanical deformation, thermal tuning[21,22], phase-change materials[23–25], micro-electromechanical systems[26], and electro-optic effects[27,28]. Among these methods, liquid crystal (LC)-based modulation stands out as especially advantageous for visible and near-infrared applications, owing to its low optical losses, relatively fast response times on the order of milliseconds, and convenient voltage-driven control mechanisms (Comparison of reported tunable metalenses are shown in Table S1 in Supplementary information of Section 1)[29–33].

While recent work has shown that rotational point-spread functions generated by static metasurfaces can be used for depth sensing, these devices lack in-situ tunability and cannot seamlessly switch between high-resolution imaging and depth-encoded operation[34–37]. Addressing this gap requires a single platform that combines multifunctionality, depth retrieval, and high-resolution imaging, with rapid electronic control.

Here, we propose an electrically tunable metalens that leverages hydrogenated amorphous silicon (*a*-Si:H) meta-atoms combined with an integrated LC cell for rapid and precise polarization control. The metalens incorporates both propagation and geometric phase profiles, enabling independent manipulation of left-circularly polarized (LCP) and right-circularly polarized (RCP) incident beams. Specifically, under LCP illumination, the metalens produces a double-helix-shaped focal pattern, while under RCP illumination, it provides an extended depth-of-focus (DOF). This polarization-dependent behavior allows the metalens to simultaneously achieve high-resolution imaging and extensive depth sensing within a single optical component.

Moreover, when the incident beam contains both polarization states simultaneously, distinct and rotated focal spots emerge, encoding depth information directly into the optical field. By analyzing rotation angles, we demonstrate precise depth retrieval, thereby transforming the metalens into a versatile depth-sensing and imaging platform. Finally, we validate the metalens on biologically relevant specimens including a rubber-tree leaf, a skeletal-muscle cross-section, and a live planarian. Accurate, color-coded depth maps spanning roughly 90 μm are retrieved, demonstrating the device's practical utility for complex, scattering tissues. The use of an electrically driven LC cell enables rapid switching between these polarization states, highlighting its potential for real-time, dynamic imaging and adaptive optics applications.

Overall, the presented electrically tunable metalens represents a compact and multifunctional optical solution, merging polarization-sensitive high-resolution imaging capabilities with advanced depth-sensing features. Its versatile, LC-based reconfigurability holds significant promise for diverse applications, including biomedical imaging, optical communications, three-dimensional displays, and advanced microscopy systems.

Theory and design

Designing the dual-mode metalens

The dual-mode metalens was designed to enable polarization-sensitive focal patterns, aiming to overcome the conventional trade-off between imaging depth range and resolution. By carefully engineering two distinct polarization-dependent phase profiles, the metalens can generate a double-helix focal distribution under LCP beam and an extended DOF under RCP beam, as illustrated in Fig. 1(a) and 1(d), respectively.

Under LCP illumination, the required phase mask (φ_{LCP}) was composed by combining two separate components shown in Fig. 1(b): a hyperbolic lens phase profile (φ_{f0}) and a two-fold self-rotating phase profile (φ_{rot}). The hyperbolic lens phase (φ_{f0}) is described by the following equation[38,39]:

$$\varphi_{f0}(x,\ y) = \frac{2\pi}{\lambda} \cdot \left(f_0 - \sqrt{x^2 + y^2 + f_0^2}\right) , \tag{1}$$

where λ denotes the target wavelength of the incident light (635 nm in this study), f_0 denotes the focal length (= 2 mm), and x and y are the Cartesian coordinates on the metasurface plane. The metasurface had a diameter of 500 μm, corresponding to a numerical aperture of 0.13.

The two-fold self-rotating phase profile (φ_{rot}) is expressed by[40–42]:

$$\varphi_{\mathrm{rot}}(r, \theta) = k \cdot \mathrm{round}\left(a \cdot r^b\right) \cdot \left(\theta + \frac{\pi}{2}\right) , \tag{2}$$

where k is controlled parameter for the lobe number for the splitting patterns, r represents the radial coordinate ($r = \sqrt{x^2 + y^2}$), θ indicates the azimuth angle ($\theta = \tan^{-1}\left(\frac{y}{x}\right)$) , a regulates the tail of the rotating beam, and b modified the overall phase pattern. A detailed parametric sweep was performed to identify optimal values for a and b, carefully evaluating the intensity at circular points, circularity, number of circles, Euler number, and rotation angle. The optimal values were found to be a = 0.65 and b = 1, with full parametric analysis and optimization criteria detailed in Supplementary information of Section 2. Additionally, simulated maximum intensity distributions and rotation angle characteristics over the range z = 1.9 mm to z = 2.1 mm using these optimal parameters are provided in Supplementary information of Section 3. Normalized intensity distributions around the designed focal plane (from z = 1.92 mm to z = 2.08 mm) under LCP illumination clearly illustrate the rotating double-helix pattern (Fig. 1(c)).

For RCP illumination, the phase mask (φ_{RCP}) was

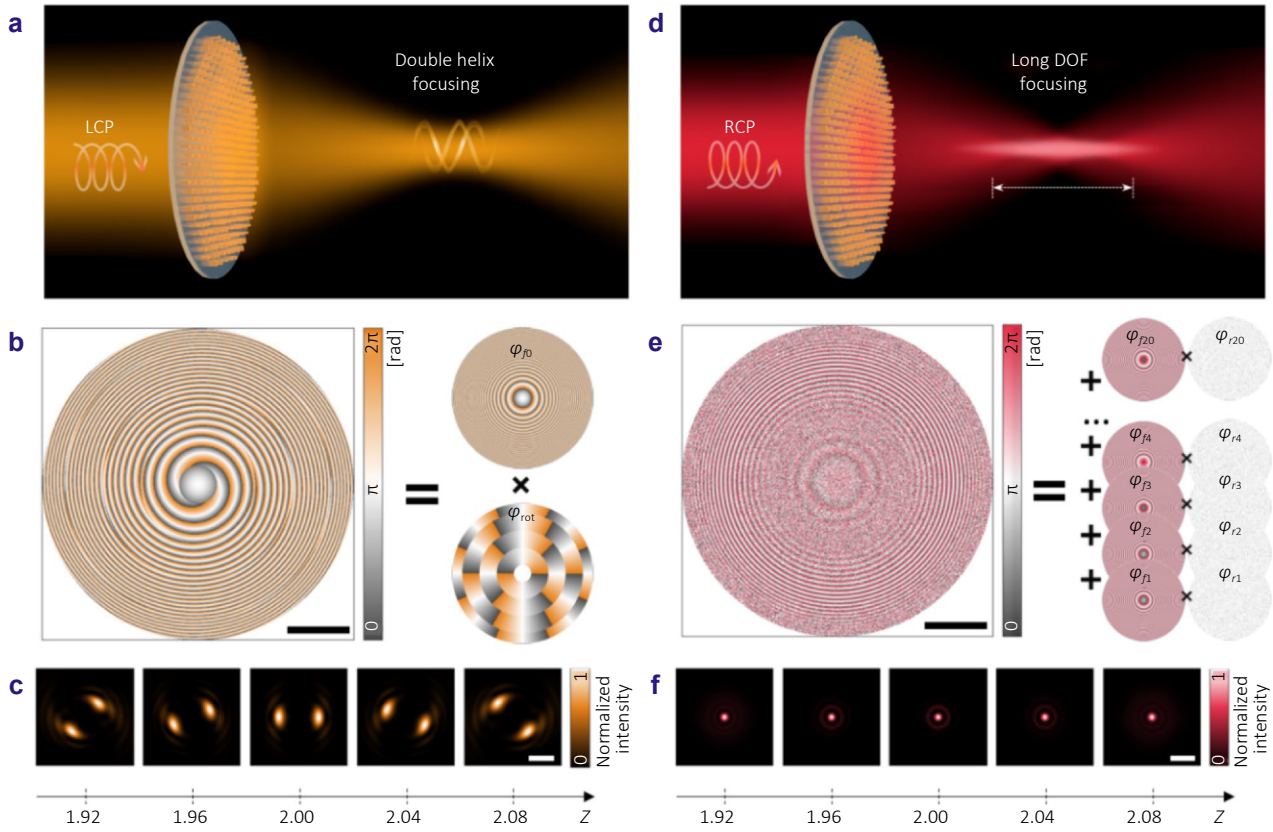

Fig. 1 | Dual-mode polarization-sensitive metalens enabling double-helix focusing (LCP illumination) and extended depth-of-focus (RCP illumination). (a) Schematic showing the metalens under LCP illumination, generating a double-helix focal pattern. (b) Phase mask design for LCP illumination, composed by combining a hyperbolic lens phase (φ_{f0}) with focal length f = 2 mm and a two-fold self-rotating phase profile (φ_{rot}). Black scale bar: 100 μm. (c) Normalized intensity distributions around the designed focal plane (from z = 1.92 mm to z = 2.08 mm) for LCP illumination, illustrating the rotation of two distinct PSFs. White scale bar: 10 μm. (d) Schematic of the metalens under RCP illumination, producing a single PSF with an extended DOF. (e) Phase mask construction for RCP illumination. The mask is generated by combining 20 pairs of elements; each pair consists of a hyperbolic lens phase (φ_{f1}, φ_{f2}, ... , φ_{f20}) with varying focal lengths, multiplied by corresponding random binary masks (φ_{r1}, φ_{r2}, ... , φ_{r20}), where at each pixel position exactly one mask has a value of 1, and the other 19 masks are 0. Black scale bar: 100 μm. (f) Normalized intensity distributions under RCP illumination within the same axial range, demonstrating a consistent, narrow FWHM PSF maintained across the extended focal region. White scale bar: 10 μm.

constructed by summing 20 distinct pairs of elements in Fig. 1(e), each pair containing a hyperbolic lens phase with varying focal lengths and corresponding random binary masks[43,44]. The hyperbolic lens phases (φ_{f1},φ_{f2} ..., φ_{f20}) were defined by:

$$\varphi_{fn}(x,\ y) = \frac{2\pi}{\lambda} \cdot \left(f_n - \sqrt{x^2 + y^2 + f_n^2}\right),\ n = 1, 2, \cdots, 20\ . \tag{3}$$

The focal lengths (f_n) were systematically calculated starting from a central focal length f_0, using carefully selected parameters: the total 20 focal points with 10 μm inter-focal spacing. This allowed precise axial positioning of the resulting focal points.

The corresponding random binary masks (φ_{r1}, φ_{r2}, ... , φ_{r20}) were generated such that at each pixel position only one mask had a value of 1 and the others were set to 0. This selection process was mathematically expressed as:

$$\varphi_{fn}(x,\ y) = \begin{cases} 1, \text{if mask } k \text{ is assigned to pixel}(x, y) \\ 0, \text{otherwise} \end{cases}\ . \quad k = 1, 2, \cdots, 20 \tag{4}$$

This structured combination of phase elements resulted in a consistent and extended depth-of-focus for RCP illumination. Normalized intensity distributions under RCP illumination within the axial range from z = 1.92 mm to z = 2.08 mm (Fig. 1(f)) demonstrate a single, narrow full-width-half-maximum (FWHM) PSF consistently maintained along the extended focal region. Uniformity of the RCP extended-DOF was verified numerically by sweeping the detection plane from 1.90 mm to 2.10 mm in 10 μm steps. (See Supplementary information of Section 9 for the x-z map, lateral line profiles, and focal-plane PSFs.) This sophisticated design strategy provides distinct and stable focal modes selectively activated by controlling the polarization state of the incident beam. This design approach provides a unique capability where LCP illumination creates a rotating

double-helix PSF pattern near the focal plane, while RCP illumination produces an extended DOF with a consistently narrow PSF.

Meta-atom simulation and fabrication

The design of the meta-atom was essential for achieving the dual-mode metalens with differing focal responses for LCP and RCP light. Figure 2(a) illustrates that rectangular *a*-Si:H pillars were chosen for the meta-atoms owing to their elevated transmittance and a measured complex refractive index of 2.9529 + 0.0095i at 635 nm, as specified in Supplementary information of Section 4.

The designed meta-atoms had a fixed height H = 600 nm and periodicity P = 300 nm, fabricated on a fused silica substrate. Rigorous coupled-wave analysis (RCWA) was employed to perform parameter sweeps over the meta-atom dimensions along the x and y directions (L_x and L_y), varying from 50 nm to 250 nm. This design approach leveraged both propagation and geometric (Pancharatnam-Berry) phases, enabling independent manipulation of LCP and RCP light within a single metasurface.

Each rectangular meta-atom acts effectively as a half-wave plate, requiring a phase retardation difference $|\phi_x - \phi_y| \approx \pi$, where ϕ_x and ϕ_y are phase delays for x- and y-polarized incident light, respectively. For simplicity, the propagation phase $\varphi_{\text{prop}}(x, y)$ was assumed equivalent to ϕ_x. By rotating

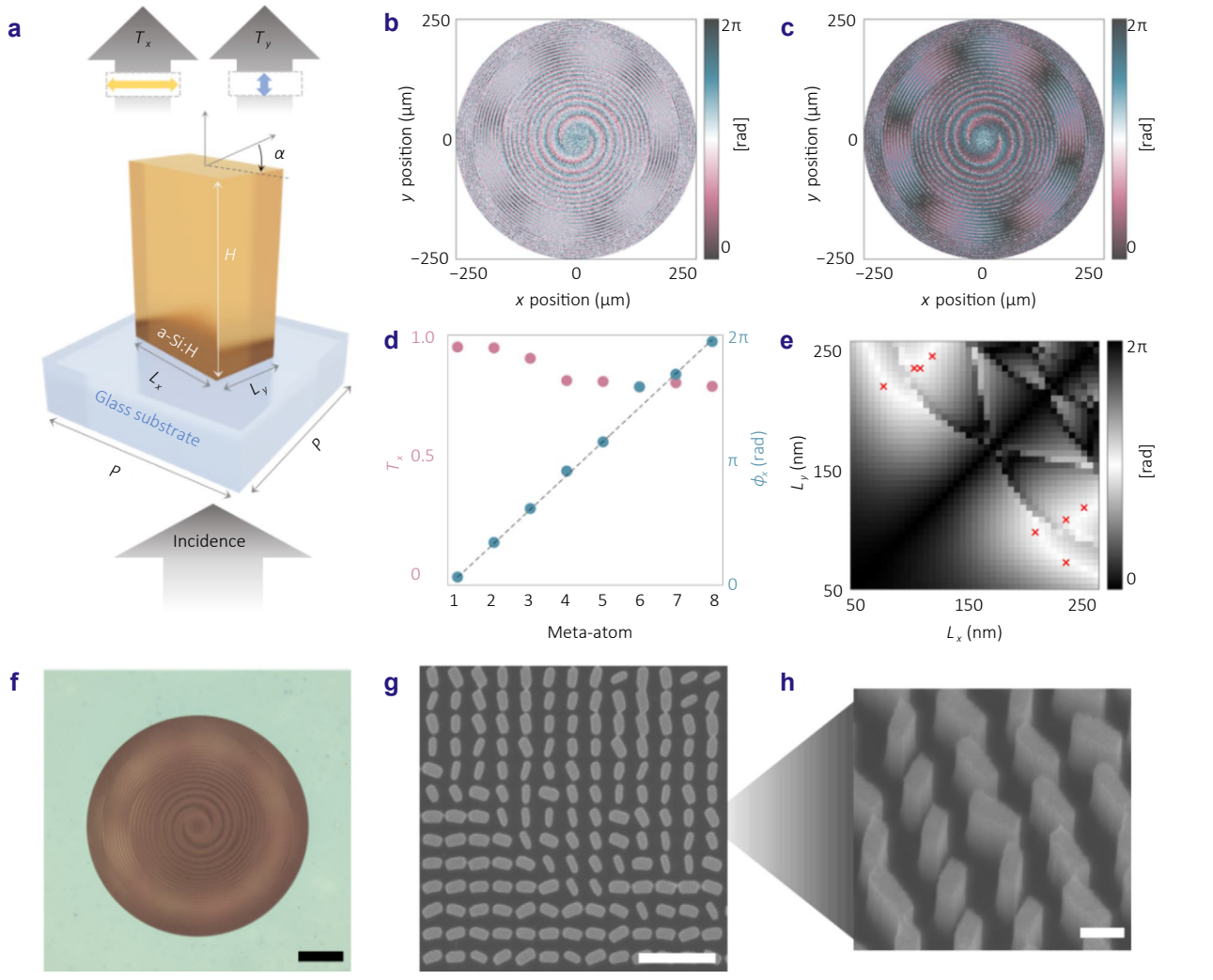

Fig. 2 | Simulation and fabrication results for meta-atom design. (a) Geometric definition of the meta-atom: P, L_x, L_y, H, and ϑ, and the corresponding transmittances (T_x, T_y) for x- and y-polarized incidence. (b) Required propagation phase map according to the spatial position on the metalens. (c) Required geometric phase map according to the spatial position on the metalens. (d) Transmittance and phase profiles of eight selected fundamental meta-atoms that collectively cover the full 0 to 2π phase range. (e) Calculated phase difference ($\Delta\Phi$) map as L_x and L_y, vary from 50 nm to 250 nm, highlighting a near-π phase difference. Positions of the eight fundamental meta-atoms are marked with red '×'. (f) Optical microscope image of the fabricated metalens. Black scale bar = 100 μm. (g) Top-view SEM image of the fabricated metalens. White scale bar = 1 μm. (h) Tilted-view SEM image showing the structural details of fabricated meta-atoms. White scale bar = 200 nm.

each meta-atom at an angle α, a geometric phase $\varphi_{\text{geo}}(x,y)$ equal to twice the rotation angle 2α, was imparted with opposite signs for LCP and RCP illumination.

To independently control LCP and RCP illumination responses, both propagation and geometric phases must be combined. Mathematically, the total phases for LCP and RCP illumination can be expressed as:

$$\varphi_{\text{LCP}}(x,y) = \varphi_{\text{prop}}(x,y) + \varphi_{\text{geo}}(x,y) \ , \tag{5}$$

$$\varphi_{\text{RCP}}(x,y) = \varphi_{\text{prop}}(x,y) - \varphi_{\text{geo}}(x,y) \ . \tag{6}$$

These equations yield:

$$\varphi_{\text{prop}}(x,y) = \frac{\varphi_{\text{LCP}}(x,y) + \varphi_{\text{RCP}}(x,y)}{2} \ , \tag{7}$$

$$\varphi_{\text{geo}}(x,y) = \frac{\varphi_{\text{LCP}}(x,y) - \varphi_{\text{RCP}}(x,y)}{2} \ . \tag{8}$$

The corresponding required propagation and geometric phases are shown in Fig. 2(b) and 2(c), extracted directly from the designed metalens profiles. The propagation phase was discretized into eight fundamental meta-atoms, carefully selected to uniformly span the 0 to 2π phase range. Figure 2(d) presents the transmittance and corresponding phase profiles of these eight selected fundamental meta-atoms, indicating high transmittance (~0.88 average) and good agreement with the desired linear phase distribution (dashed line).

The calculated phase difference $\Delta\phi$ as L_x and L_y vary from 50 nm to 250 nm is shown in Fig. 2(e), highlighting a robust near-π phase difference. Positions of the selected fundamental meta-atoms are marked with red '×' symbols. Detailed geometrical parameters L_x and L_y for each meta-atom are summarized in Supplementary information of Section 5. Also, Supplementary information of Section 6 contains further data on transmittance and phase delay as L_x and L_y are varied.

Fabrication of the designed metalens followed standard electron-beam lithography and reactive-ion etching processes. Initially, a 600 nm-thick *a*-Si:H film was deposited onto a silica substrate using plasma-enhanced chemical vapor deposition, with specific gas flows of SiN_4 (10 sccm) and H_2 (75 sccm) at 300 °C and 40 mTorr. Subsequently, a positive-tone resist (ZEP520A) was spin-coated and patterned using an electron-beam lithography system (Elionix ELS-7800, 100 pA). A 60 nm-thick Cr layer was evaporated as an etching mask, followed by lift-off. The pattern was transferred onto the *a*-Si:H layer by inductively coupled reactive-ion etching (ICP-RIE) using the Cr mask. Residual Cr was removed with an etchant solution (ETCR-400, APCT). Scanning electron microscopy (SEM) from Hitachi (Regulus 8100, 7 kV) and optical microscopy (Olympus MX63, 20× magnification) confirmed successful fabrication and structural integrity of the metalens. Optical microscopy images (Fig. 2(f)) and SEM images (Fig. 2(g–h)) confirm the structural fidelity and precision of the fabricated meta-atoms. The high-resolution SEM images clearly show the uniformity and accuracy achieved in the fabrication process, essential for realizing the targeted optical performance.

Results and discussion

Characterization of the polarization-sensitive focusing properties of the metalens

To evaluate the focusing properties of the electrically-tunable polarization-sensitive metalens, experimental characterizations were performed under varying polarization conditions. Figure 3(a) illustrates the experimental setup, consisting of a 635 nm laser source whose beam was expanded via a custom beam expander. The polarization state of the incident beam was precisely controlled by employing a LC cell in combination with a linear polarizer (LP), as detailed in Fig. 3(b). Specifically, applying a voltage of 1.4 V to the LC cell resulted in LCP incident beam. Increasing the voltage to 1.9 V converted the incident polarization to RCP. A function generator (SIGLENT, Agilent 33220A) facilitated rapid voltage modulation, enabling quick switching between LCP and RCP states. The fully integrated system, wherein the metalens and LC cell were assembled onto a transparent substrate, is shown in Fig. S6 in Supplementary information of Section 7.

The LC modulator fabrication involved initially applying polyimide (Nissan Chemical, Korea) onto glass substrates. The polyimide was spin-coated at speeds of 1000 rpm for 10 s followed by 2500 rpm for 30 s, resulting in a measured thickness of approximately 182 nm. Subsequently, the coated plates were heated at 230 °C for 60 min and rubbed to achieve uniform liquid crystal alignment. Two glass plates were combined with a precise 10 μm spacer using UV glue (Norland Optical Adhesive 65). The resulting sandwich structure was then filled with 5CB (4-Cyano-4'-pentylbiphenyl) liquid crystals. The final LC cell was attached to the metalens substrate using UV adhesive and electrically connected to the function generator for effective voltage modulation.

The focusing performance was characterized using an optical imaging system composed of a 50× objective lens, tube lens (TL), quarter-wave plate (QWP), LP, and a CCD camera, mounted on a motorized *z*-axis translation stage to facilitate axial scanning. Detailed information of optical components and image-processing latency analysis for real-time feasibility is explained in Supplementary information of Section 8. Under LCP illumination (Fig. 3(c–f)), axial intensity distributions, generated by stacking *xz*-plane intensities at $y = 0$ (from $z = 1.8$ mm to $z = 2.2$ mm), showed the expected double-helix focusing behavior (Fig. 3(c)). To quantify spatial resolution, the point-spread function (PSF) was analyzed in both lateral and axial directions. The axial

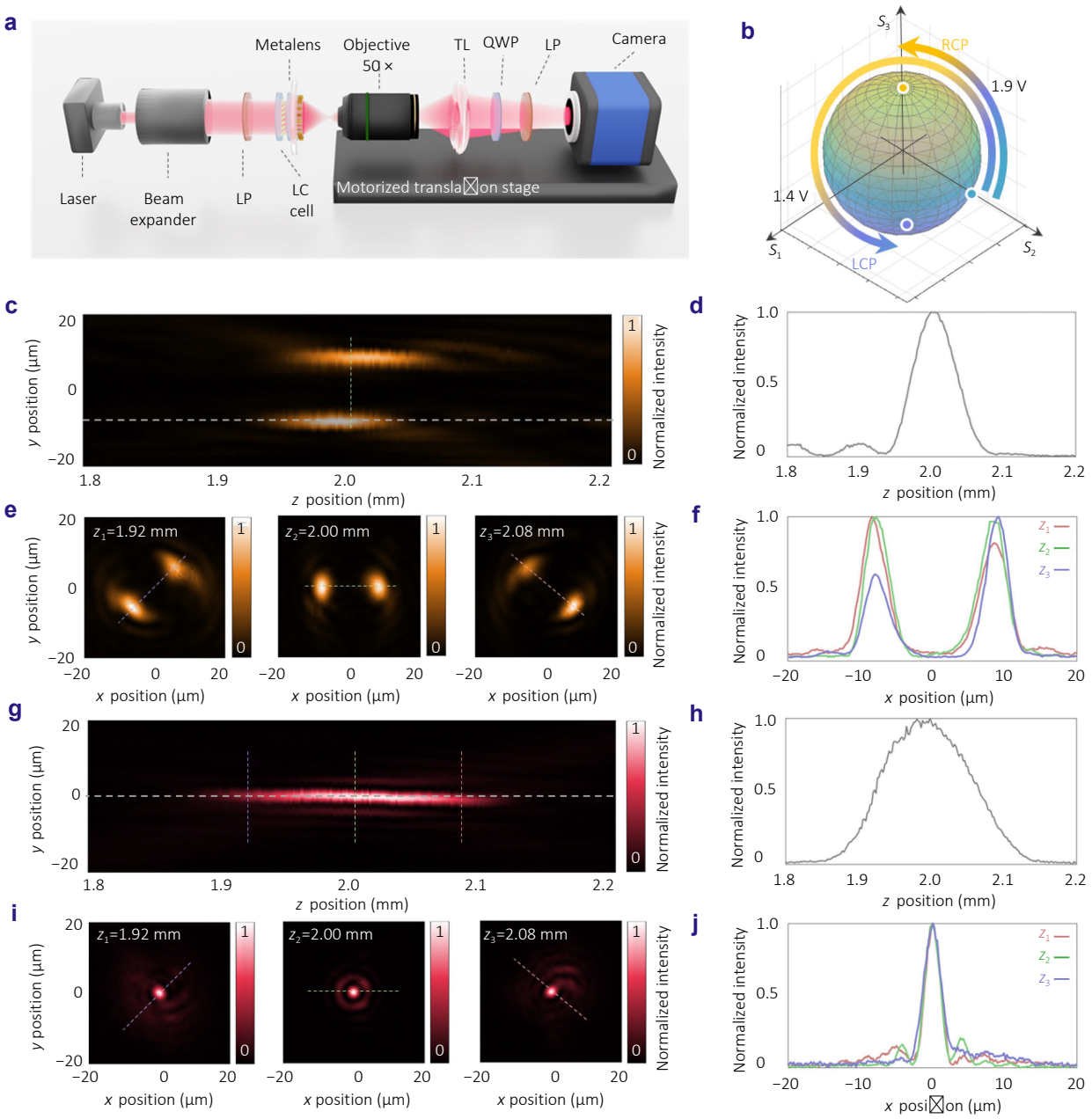

Fig. 3 | Characterization of the focusing properties of the metalens. (a) Schematic diagram of the optical setup used for focusing characterization. (b) Poincaré sphere illustrating polarization state transitions controlled by liquid crystal (LC) from LCP (at 1.4 V) to RCP (at 1.9 V) illumination. (c) Axial intensity distribution (*xz*-plane stacking at $y = 0$) under LCP illumination, scanned from $z = 1.8$ mm to $z = 2.2$ mm. (d) Axial line profile at a single PSF to determine axial resolution; measured FWHM ≈ 74.4 μm. (e) Focal-plane intensity distributions at three selected axial positions ($z_1 = 1.92$ mm, $z_2 = 2.00$ mm, $z_3 = 2.08$ mm). (f) Lateral intensity profiles connecting two PSFs to estimate lateral resolution; FWHM at $z_2 \approx 3.6$ μm. (g) Axial intensity distribution (*xz*-plane stacking at $y = 0$) under RCP illumination, scanned from $z = 1.8$ mm to $z = 2.2$ mm. (h) Axial line profile at a single PSF under RCP illumination to determine axial resolution; measured FWHM ≈ 148.6 μm. (i) Focal-plane intensity distributions under RCP illumination at three axial positions ($z_1 = 1.92$ mm, $z_2 = 2.00$ mm, $z_3 = 2.08$ mm). (j) Lateral intensity profile at the same angular orientation as (f), used to estimate lateral resolution under RCP; FWHM at $z_2 \approx 2.5$ μm. Lateral profiles in (f) and (j) are uniformly normalized to the peak intensity at z_2 to allow direct comparison across planes.

resolution, determined from line scanning along the *z*-axis through a single PSF, yielded a FWHM of approximately 74.4 μm (Fig. 3(d)). Focal-plane intensity profiles at three axial positions ($z_1 = 1.92$ mm, $z_2 = 2.00$ mm, $z_3 = 2.08$ mm) are presented in Fig. 3(e). Analysis of the lateral resolution, based on intensity profiles connecting two PSFs, indicated an FWHM of roughly 3.6 μm at position z_2 (Fig. 3(f)).

Under RCP illumination (Fig. 3(g–j)), the metalens displayed a significantly extended depth-of-focus. Axial intensity distributions from identical scanning conditions

(from z = 1.8 mm to z = 2.2 mm) confirmed the extended focal region (Fig. 3(g)). Axial line scans through the PSF provided an axial resolution estimate with an FWHM of approximately 148.6 μm (Fig. 3(h)). Focal-plane intensity distributions at representative axial positions are shown in Fig. 3(i). The lateral resolution was evaluated at an orientation comparable to the LCP illumination condition, yielding an FWHM of about 2.5 μm at position z_2, as detailed by the line scan in Fig. 3(j). For a fair comparison, all lateral profiles in Fig. 3(f) and 3(j) are now normalized to the same reference, the peak intensity at z_2, recorded under identical illumination and exposure.

The experimental results confirm that the electrically-tunable polarization-sensitive metalens attains near diffraction-limited resolution along its optimized axes, closely aligning with theoretical predictions, while deliberately incorporating particular axial and lateral resolution attributes to enhance advanced depth-sensing and imaging capabilities. Simulated data corresponding to Fig. 3(c–j) are provided in Fig. S8 in Supplementary information of Section 9, demonstrating agreement between experimental and simulated results. The discrepancies between the simulation and experimental data are attributed to fabrication defects and measurement errors. The slight intensity imbalance between the two PSF lobes under LCP illumination observed at z_1 and z_3 is attributed mainly to fabrication deviations that round and occasionally merge the designed rectangular posts, with a smaller contribution from residual alignment error during axial scanning. A side-by-side comparison of PSFs from a sub-optimal and the best device, highlighting the impact of fabrication quality on lobe balance and rotational fidelity, is shown in Supplementary information of Section 10.

Depth imaging characterization using the electrically tunable metalens

To evaluate the depth-sensing capability of the metalens with extended focal characteristics, imaging experiments were conducted as illustrated in Fig. 4(a). The experimental setup consisted of a 4*f* imaging system, where a 10× objective lens and the designed metalens were employed. The axial displacement of the focal plane (Δz) relative to the metalens was precisely controlled using a translation stage to adjust the distance between the objective lens and the customized imaging target. Due to the magnification of the 10× objective lens, the image projected onto the metalens was reduced by a factor of ten compared to the original target dimensions. To validate the imaging performance accurately, we used a specially fabricated custom-designed target.

The method for extracting depth information using the electrically tunable dual-mode metalens is depicted in Fig. 4(b). Images captured under LCP illumination exhibit two distinct and rotated target shapes, whereas images obtained under RCP illumination yield a single image with superior spatial resolution. Due to intrinsic fabrication imperfections and PSF distortions, images acquired under LCP illumination required correction. This correction step involved retaining the original rotation angles derived from LCP mode images and applying shape correction using the higher-resolution images captured under RCP illumination. The subsequent image processing facilitated accurate separation and refinement of the target shapes.

Following image processing, rotation angles (β) were systematically extracted. These rotation angles provided essential depth information (Δz) due to their direct correlation with axial displacement. By matching extracted rotation angles to known Δz values, precise depth estimations of the imaging targets were achieved.

Experimental results confirming this approach are demonstrated in Fig. 4(c). The X-shaped negative resolution target measures 136.7 μm in both length and width for evaluating depth imaging which are shown in Fig. 4(a). Three distinct depth positions (Δz_1 = 30.5 μm, Δz_2 = 0 μm, and Δz_3 = − 48.3 μm) were tested. Initially overlapping images obtained from LCP illumination were successfully separated and processed to yield clear angle-extracted images. These angles were subsequently matched with corresponding depths. Finally, depth information extracted from these angles was color-mapped onto the high-resolution images obtained under RCP illumination. The true stage displacements were Δz_1 = 30.0 μm, Δz_2 = 0 μm, and Δz_3 = − 50 μm, yielding absolute errors of 0.5 μm, 0 μm, and 1.7 μm, respectively. The resulting mean absolute error is 0.73 μm, or roughly 1.5% of the 80 μm full measurement span, corresponding to an axial sensitivity of ~1 μm. The resultant images shown in Fig. 4(a) highlight the robustness of the imaging approach, demonstrating consistent image quality and clear depth differentiation even across varying focal depths.

Depth-resolved imaging of biological specimens

To demonstrate that the dual-mode metalens can recover depth information from real, complex specimens, we imaged three representative biological samples: a rubber-tree leaf, a transverse section of skeletal muscle, and a live planarian. All measurements employed the same optical setup described in Fig. 4(a), and only the specimen was exchanged between acquisitions. A 10× bright-field objective provided the reference image for each sample (left-hand column in Fig. 5; black scale bar = 250 μm), after which LCP and RCP mode images were captured using the LC-integrated metalens exactly as outlined in Fig. 4. For completeness, we note that differences in sharpness relative to the 10× objective arise from intrinsic NA/PSF and throughput considerations; a quantitative analysis with simulated focal-plane PSFs is provided in Supplementary information of Seciton 11. Detailed discussion for scalability of the double-helix mode

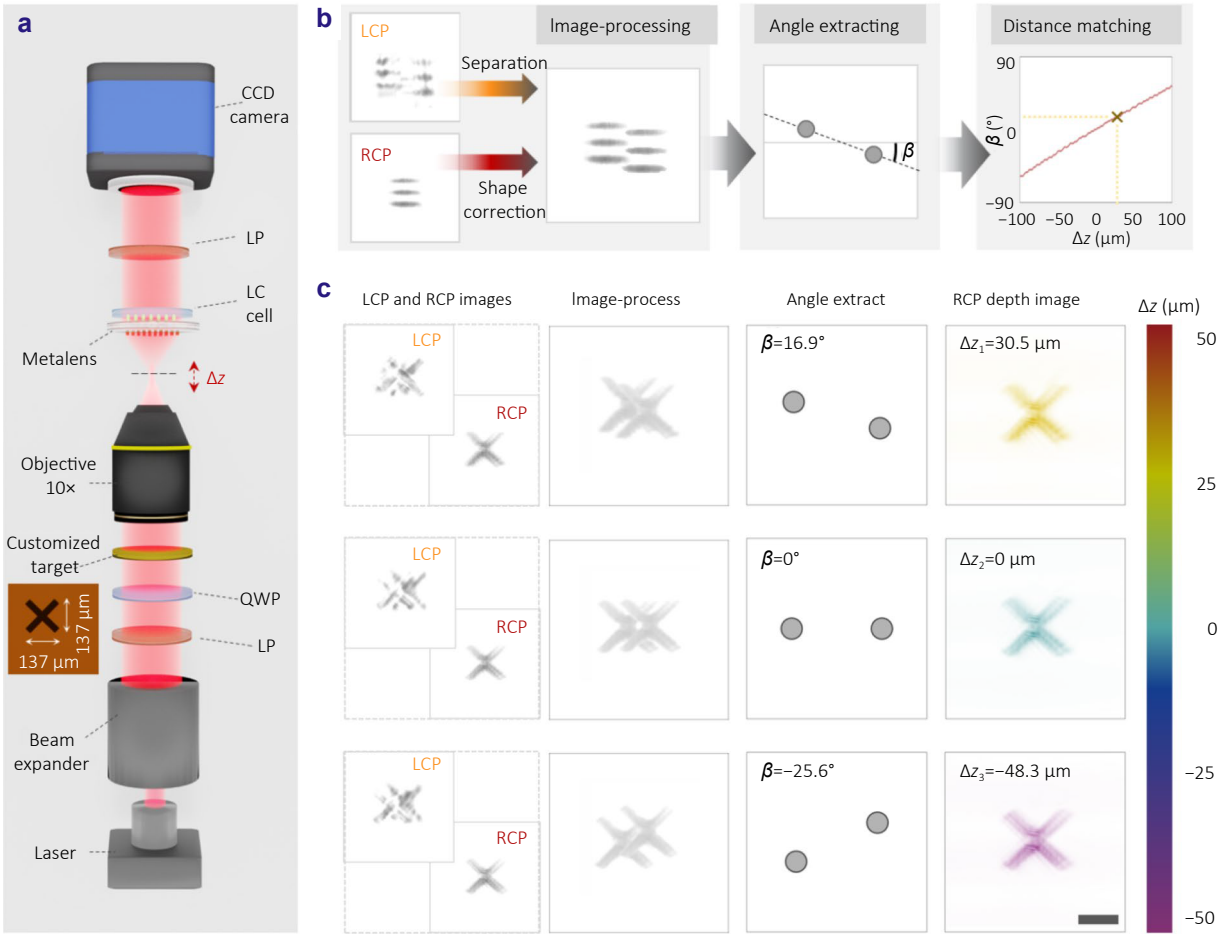

Fig. 4 | Depth imaging characterization. (a) Optical setup schematic for depth imaging characterization. Axial movement of the objective lens creates three distinct depth positions (Δ*z*). (b) The imaging process involves separating and correcting shapes from LCP and RCP mode images, extracting rotation angles, and matching these angles to depth information (Δ*z*). (c) Imaging results demonstrating successful depth extraction from processed LCP and RCP mode images at three different depth positions. Scale bar = 2 mm.

at higher NA and through-focus simulation comparing the RCP extended-depth-of-focus design with a standard *NA* = 0.13 lens are also included in Supplementary information of Section 11.

For every field of view, we recorded a pair of raw metalens images: a double-helix LCP mode image and a high-definition RCP frame. After the LCP/RCP mode images separation step, the LCP mode image was split into two images and its shape was corrected with the corresponding RCP intensity map. After yielding the rotation angle β, which was converted to an axial offset Δz via the calibration curve established in Fig. 4(b). The resulting depth values (+42.1 μm, 0 μm, and −46.9 μm for the three examples) are reported alongside the extracted angles. Finally, each high-resolution RCP image was color-coded according to Δz using the hue scale shown at the right of Fig. 5 (white scale bar = 2 μm).

These results confirm that the metalens can recover depth over a ~90 μm range in heterogeneous, light-scattering tissues while preserving sub-cellular lateral detail. Because the LC modulator switches polarization in milliseconds, the same device can rapidly alternate between depth-encoded and conventional high-resolution imaging modes, making it attractive for live-cell microscopy, histological inspection, and compact endoscopic probes. Supplementary information of Section 7 describes the analysis of thermal robustness and tuning speed.

Conclusions

In this study, we have successfully demonstrated an electrically tunable dual-mode metalens capable of generating polarization-sensitive focal patterns, effectively addressing the longstanding trade-off between depth-of-focus and imaging resolution. By precisely engineering phase profiles for LCP and RCP illumination, the metalens produces distinctive optical responses: a rotating double-helix PSF under LCP illumination and an extended DOF with a

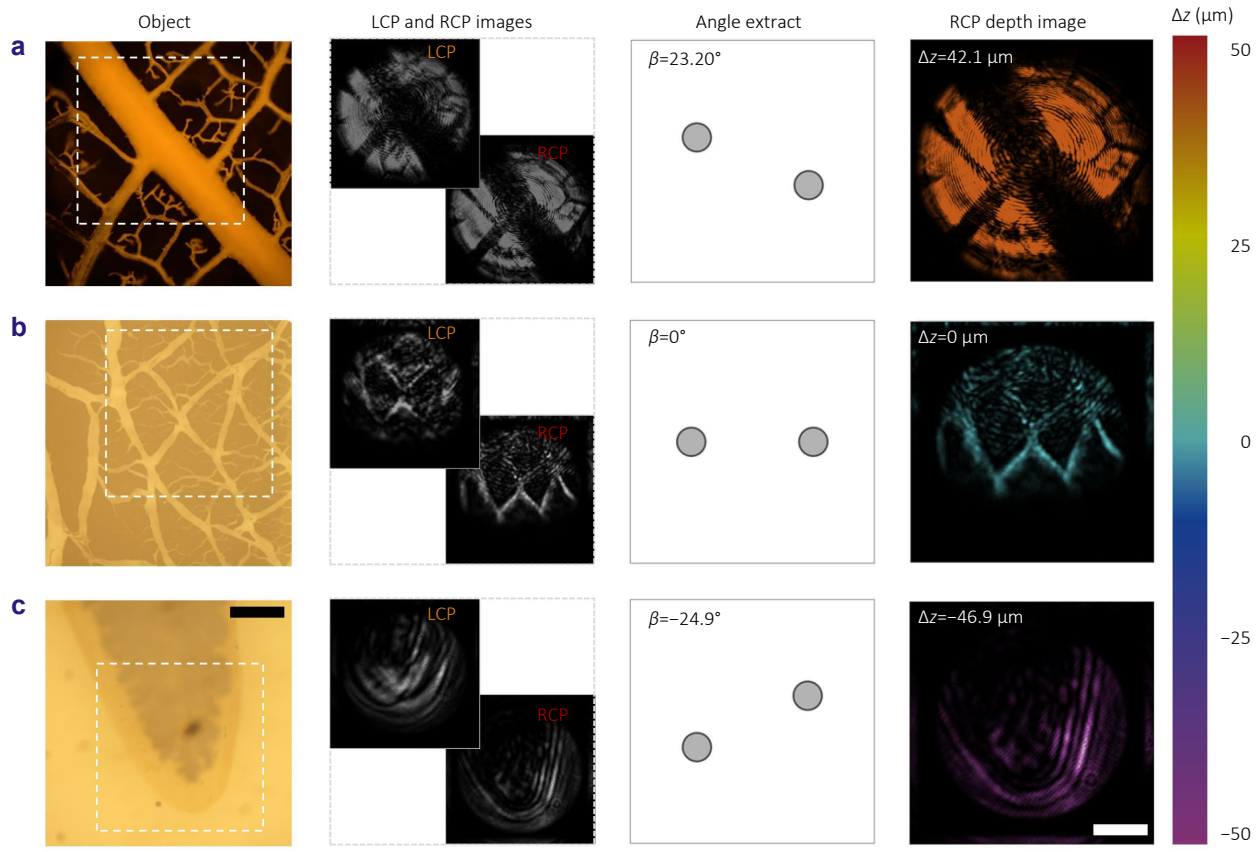

Fig. 5 | Depth-resolved imaging of biological specimens using the dual-mode metalens. Rows show (a) rubber-tree leaf, (b) skeletal-muscle cross-section, and (c) planarian, each imaged at three axial offsets Δ*z*. Left: 10× bright-field reference (black bar = 250 μm). Middle: LCP (upper) and RCP (lower) mode metalens views used to extract rotation angle *θ*. Right: RCP images color-mapped to depth (white bar = 2 μm), revealing sample structure at the retrieved axial positions.

narrow PSF under RCP illumination. This dual functionality enables the metalens to simultaneously achieve wide depth sensing range and high lateral resolution, significantly enhancing its applicability in advanced imaging systems.

The meta-atom structures, fabricated from low-loss *a*-Si:H, were meticulously designed using RCWA, enabling precise manipulation of propagation and geometric phases. Experimental characterization validated near-diffraction-limited performance with close alignment to theoretical predictions. High-resolution SEM and optical microscopy imaging confirmed excellent fabrication fidelity.

Comprehensive experimental assessments demonstrated that the metalens provided robust imaging performance under varied polarization conditions, highlighting its capability for rapid polarization switching via an integrated LC modulator. The depth-sensing experiments further verified that the engineered focal profiles facilitated reliable extraction of depth information through the rotation angles of dual image patterns under LCP illumination, subsequently refined by high-resolution RCP imagery.

Overall, the electrically tunable dual-mode metalens represents a promising optical platform, merging depth-sensitive imaging and high-resolution capabilities into a compact, integrated device. Its proven performance on real bio-samples, combined with rapid electronic control, paves the way for applications in biomedical imaging, 3-D microscopy, optical sensing, and adaptive optics[32,45,46].

References

1. Moon SW, Kim Y, Yoon G et al. Recent progress on ultrathin metalenses for flat optics. *iScience* **23**, 101877 (2020).
2. Li B, Piyawattanametha W, Qiu Z. Metalens-based miniaturized optical systems. *Micromachines* **10**, 310 (2019).
3. Liang HW, Martins A, Borges BHV et al. High performance metalenses: numerical aperture, aberrations, chromaticity, and trade-offs. *Optica* **6**, 1461–1470 (2019).
4. Khorasaninejad M, Chen WT, Devlin RC et al. Metalenses at visible wavelengths: diffraction-limited focusing and subwavelength resolution imaging. *Science* **352**, 1190–1194 (2016).
5. Jung C, Kim G, Jeong M et al. Metasurface-driven optically variable devices. *Chem Rev* **121**, 13013–13050 (2021).
6. Chen HT, Taylor AJ, Yu NF. A review of metasurfaces: physics and applications. *Rep Prog Phys* **79**, 076401 (2016).
7. Bukhari SS, Vardaxoglou J, Whittow W. A metasurfaces review: definitions and applications. *Appl Sci* **9**, 2727 (2019).

8. Noh J, Kim J, Rho J. Overcoming information sparsity in metasurfaces for full-color holography via end-to-end design. *Nano Lett* **25**, 11398–11405 (2025).
9. Moon S, Kim S, Kim J et al. Single-layer waveguide displays using achromatic metagratings for full-colour augmented reality. *Nat Nanotechnol* **20**, 747–754 (2025).
10. Jeon D, Shin K, Moon SW et al. Recent advancements of metalenses for functional imaging. *Nano Converg* **10**, 24 (2023).
11. Pan MY, Fu YF, Zheng MJ et al. Dielectric metalens for miniaturized imaging systems: progress and challenges. *Light Sci Appl* **11**, 195 (2022).
12. Liu WW, Cheng H, Tian JG et al. Diffractive metalens: from fundamentals, practical applications to current trends. *Adv Phys X* **5**, 1742584 (2020).
13. Yang Y, Kang D, Seong J et al. Mechanically robust and self-cleanable encapsulated metalens via spin-on-glass packaging. *Microsyst Nanoeng* **11**, 118 (2025).
14. Choi M, Kim J, Moon S et al. Roll-to-plate printable RGB achromatic metalens for wide-field-of-view holographic near-eye displays. *Nat Mater* **24**, 535–543 (2025).
15. Kim J, An J, Kim W et al. Large-area floating display with wafer-scale manufactured metalens arrays. *Laser Photonics Rev* **19**, 2401425 (2025).
16. Cui T, Bai BF, Sun HB. Tunable metasurfaces based on active materials. *Adv Funct Mater* **29**, 1806692 (2019).
17. Zhu WM, Liu AQ. Tunable chiral metasurfaces. In Zhu WM, Liu AQ. *Metasurfaces: Towards Tunable and Reconfigurable Meta-Devices* 91–111 (Springer, Singapore, 2023).
18. Abdelraouf OAM, Wang ZY, Liu HL et al. Recent advances in tunable metasurfaces: materials, design, and applications. *ACS Nano* **16**, 13339–13369 (2022).
19. Badloe T, Lee J, Seong J et al. Tunable metasurfaces: the path to fully active nanophotonics. *Adv Photonics Res* **2**, 2000205 (2021).
20. Ding F, Meng C, Bozhevolnyi SI. Electrically tunable optical metasurfaces. *Photonics Insights* **3**, R07 (2024).
21. Liao Y, Fan YL, Lei DY. Thermally tunable binary-phase VO_2 metasurfaces for switchable holography and digital encryption. *Nanophotonics* **13**, 1109–1117 (2024).
22. Xu N, Liang YY, Hao Y et al. A thermal tuning meta-duplex-lens (MDL): design and characterization. *Nanomaterials* **10**, 1135 (2020).
23. Bai W, Yang P, Wang S et al. Actively tunable metalens array based on patterned phase change materials. *Appl Sci* **9**, 4927 (2019).
24. Farmakidis N, Youngblood N, Li X et al. Plasmonic nanogap enhanced phase-change devices with dual electrical-optical functionality. *Sci Adv* **5**, eaaw2687 (2019).
25. Wang Q, Rogers ETF, Gholipour B et al. Optically reconfigurable metasurfaces and photonic devices based on phase change materials. *Nat Photonics* **10**, 60–65 (2016).
26. Ding F, Deng YD, Meng C et al. Electrically tunable topological phase transition in non-Hermitian optical MEMS metasurfaces. *Sci Adv* **10**, eadl4661 (2024).
27. Shirmanesh GK, Sokhoyan R, Wu PC et al. Electro-optically tunable multifunctional metasurfaces. *ACS Nano* **14**, 6912–6920 (2020).
28. Xie ZT, Wu JY, Fu HY et al. Tunable electro- and all-optical switch based on epsilon-near-zero metasurface. *IEEE Photonics J* **12**, 4501510 (2020).
29. Fan CY, Chuang TJ, Wu KH et al. Electrically modulated varifocal metalens combined with twisted nematic liquid crystals. *Opt Express* **28**, 10609–10617 (2020).
30. Badloe T, Kim I, Kim Y et al. Electrically tunable bifocal metalens with diffraction-limited focusing and imaging at visible wavelengths. *Adv Sci* **8**, 2102646 (2021).
31. Bosch M, Shcherbakov MR, Won K et al. Electrically actuated varifocal lens based on liquid-crystal-embedded dielectric metasurfaces. *Nano Lett* **21**, 3849–3856 (2021).
32. Kim Y, Lee J, Yeo WH et al. Rapid polarization-controlled depth sensing and imaging with an electrically tunable metalens. *Nano Lett* **25**, 9394–9401 (2025).
33. Kang D, Heo H, Yang Y et al. Liquid crystal-integrated metasurfaces for an active photonic platform. *Opto-Electron Adv* **7**, 230216 (2024).
34. Jin CQ, Zhang JH, Guo CL. Metasurface integrated with double-helix point spread function and metalens for three-dimensional imaging. *Nanophotonics* **8**, 451–458 (2019).
35. Wang FM, Lai JK, Liu HJ et al. Double helix point spread function with variable spacing for precise 3D particle localization. *Opt Express* **31**, 11680–11694 (2023).
36. Yang SW, Wei QS, Zhao RZ et al. Realizing depth measurement and edge detection based on a single metasurface. *Nanophotonics* **12**, 3385–3393 (2023).
37. Shen ZC, Zhao F, Jin CQ et al. Monocular metasurface camera for passive single-shot 4D imaging. *Nat Commun* **14**, 1035 (2023).
38. Tseng ML, Hsiao HH, Chu CH et al. Metalenses: advances and applications. *Adv Opt Mater* **6**, 1800554 (2018).
39. Chen MK, Wu YF, Feng L et al. Principles, functions, and applications of optical meta-lens. *Adv Opt Mater* **9**, 2001414 (2021).
40. Ke YG, Bian YF, Tang Q et al. Rotational photonic spin hall effect. *Nanophotonics* **12**, 4361–4373 (2023).
41. Berlich R, Stallinga S. High-order-helix point spread functions for monocular three-dimensional imaging with superior aberration robustness. *Opt Express* **26**, 4873–4891 (2018).
42. Niu K, Zhao SD, Liu Y et al. Self-rotating beam in the free space propagation. *Opt Express* **30**, 5465–5472 (2022).
43. Barulin A, Barulina E, Oh DK et al. Axially multifocal metalens for 3D volumetric photoacoustic imaging of neuromelanin in live brain organoid. *Sci Adv* **11**, eadr0654 (2025).
44. Zhao YT, Guo CK, Zhang YQ et al. Ultraviolet metalens for photoacoustic microscopy with an elongated depth of focus. *Opt Lett* **48**, 3435–3438 (2023).
45. Badloe T, Kim Y, Kim J et al. Bright-field and edge-enhanced imaging using an electrically tunable dual-mode metalens. *ACS Nano* **17**, 14678–14685 (2023).
46. Jung C, Lee E, Rho J. The rise of electrically tunable metasurfaces. *Sci Adv* **10**, eado8964 (2024).

Acknowledgements

This research was financially supported by the POSCO-POSTECH-RIST Convergence Research Center program funded by POSCO, and the National Research Foundation (NRF) grant (RS-2024-00462912) funded by the Ministry of Science and ICT (MSIT) of the Korean government. Y.K. acknowledges the Presidential Science fellowship funded by the MSIT of the Korean government. J.L. acknowledges the NRF Ph.D. fellowship (RS-2025-25436675) funded by the Ministry of Education (MOE) of the Korean government. X.L. acknowledges the CSC Chinese Government scholarship (202306890039). H.K. acknowledges the POSCO Asia fellowship, and the Yuhan Foundation *New Ilhan* fellowship.

Author contributions

The manuscript was written through contributions of all authors. All authors have given approval to the final version of the manuscript. J.R. conceived the idea and initiated the project. Y.K. designed the metalens, conducted simulations, and obtained experimental measurements. J.L. conducted all nanofabrication processes. H.H. helped to conduct real-object imaging. D.J., B.Y., X.L., H.K., and S.H. collaboratively deliberated on the concept and idea. W.-S.K. and Y.-K.K. constructed the liquid-crystal cell and performed material characterization. J.R. and T.B. guided the entire work.

Competing interests

The authors declare no competing financial interests.

Supplementary information

Supplementary information for this paper is available at https://doi.org/10.29026/oea.2026.250216